Kobe University Repository : Kernel

PDF issue: 2025-12-04

Gold nanopillar array with sharp surface plasmon resonances and the application in immunoassay

Yanagawa, Hiroto ; Hinamoto, Tatsuki ; Kanno, Takashi ; Sugimoto, Hiroshi ; Shioi, Masahiko ; Fujii, Minoru

(Citation)
Journal of Applied Physics,126(22):223104-223104

(Issue Date)
2019-12-14

(Resource Type)
journal article

(Version)
Version of Record

(Rights)
© 2019 Author(s). This article may be downloaded for personal use only. Any other use requires prior permission of the author and AIP Publishing. This article appeared in Journal of Applied Physics 126, 22, 223104 (2019) and may be found at at https://doi.org/10.1063/1.5119258

(URL)
https://hdl.handle.net/20.500.14094/90006756

Journal of Applied Physics

Gold nanopillar array with sharp surface plasmon resonances and the application in immunoassay

Cite as: J. Appl. Phys. **126**, 223104 (2019); https://doi.org/10.1063/1.5119258
Submitted: 09 July 2019 . Accepted: 29 November 2019 . Published Online: 12 December 2019

Hiroto Yanagawa, Tatsuki Hinamoto, Takashi Kanno, Hiroshi Sugimoto, Masahiko Shioi, and Minoru Fujii

View Online Export Citation CrossMark

ARTICLES YOU MAY BE INTERESTED IN

Design of AlGaN-based quantum structures for low threshold UVC lasers
Journal of Applied Physics **126**, 223101 (2019); https://doi.org/10.1063/1.5125256

Perfect anomalous reflection and refraction with binary acoustic metasurfaces
Journal of Applied Physics **126**, 224504 (2019); https://doi.org/10.1063/1.5124040

Photo-detecting of graphene/insulator/silicon heterojunction with direct tunneling mechanism
Journal of Applied Physics **126**, 223102 (2019); https://doi.org/10.1063/1.5125284

Lock-in Amplifiers up to 600 MHz
Zurich Instruments
Watch

© 2019 Author(s).

Journal of Applied Physics | ARTICLE | scitation.org/journal/jap

Gold nanopillar array with sharp surface plasmon resonances and the application in immunoassay

Cite as: J. Appl. Phys. **126**, 223104 (2019); doi: 10.1063/1.5119258
Submitted: 9 July 2019 · Accepted: 29 November 2019 ·
Published Online: 12 December 2019

View Online Export Citation CrossMark

Hiroto Yanagawa,[1,2] Tatsuki Hinamoto,[2] Takashi Kanno,[1] Hiroshi Sugimoto,[2] Masahiko Shioi,[3] and Minoru Fujii[2,a)]

AFFILIATIONS

[1]Technology Innovation Division, Panasonic Corporation, Yagumo-naka-machi, Moriguchi, Osaka 570-8501, Japan
[2]Department of Electrical and Electronic Engineering, Graduate School of Engineering, Kobe University, Rokkodai, Nada, Kobe 657-8501, Japan
[3]Life Solutions Company, Panasonic Corporation, Kadoma, Kadoma, Osaka 571-8686, Japan

[a)]**Author to whom correspondence should be addressed:** fujii@eedept.kobe-u.ac.jp

ABSTRACT

Nanoimprinting followed by metal deposition is a low-cost, high-throughput, and highly reproducible process for the fabrication of large-size plasmonic substrates required for commercial products. However, the plasmonic substrates prepared by the process usually have very broad surface plasmon resonances, which cannot be well reproduced by numerical simulations. The poor agreement between experiments and calculations has prevented the detailed analysis of the field enhancement behavior and the improvement of the performance as plasmonic substrates. In this work, we demonstrate that large-area plasmonic substrates with sharp surface plasmon resonances, which can be well reproduced by numerical simulations, are produced by sputter-deposition of gold (Au) on a commercially available nanoimprinted substrate. The good agreement between experiments and simulations allow us to identify the locations and field distributions of the hot spots. The angle dependence of specular reflectance and diffuse reflectance measurements in combination with numerical simulations reveal that a dipolelike bright mode and a higher-order dark mode exist at gaps between Au nanorods. Finally, we demonstrate the application of the developed plasmonic substrates for surface-enhanced fluorescence in sandwich immunoassays for the detection of influenza virus nucleoprotein. We show that the sharp resonance and the capability of precise tuning of the resonance wavelength significantly enhance the luminescence signal.

Published under license by AIP Publishing. https://doi.org/10.1063/1.5119258

I. INTRODUCTION

Plasmonic substrates are key components for surface-enhanced fluorescence (SEF) and surface-enhanced Raman scattering (SERS) to maximize the sensitivity of biosensing and bioimaging.[1–12] Elaborated metal nanostructures have been produced with very high accuracy by using state-of-the-art nanofabrication technologies such as electron-beam (EB) lithography[8,13–15] and ion beam lithography.[16] These processes are suitable for the proof-of-concept experiments and for achieving record-high enhancement factors due to the high processing accuracy. However, they are not very suitable for the production of commercial devices due to the low production throughput and the resultant high cost.

Nanosphere lithography (NSL), which uses a self-aligned 2-dimensional array of polystyrene or silica spheres as a template for the formation of metal nanostructures, is one of the high-throughput and low-cost processes to produce metal nanostructures on a large substrate without using expensive equipment.[17–25] A template of a sphere array is also used in a metal film over nanosphere (FON) process, in which a relatively thick metal film is deposited on the sphere array to produce metal nanostructures.[22,23,25] Similar to the FON process, a metal film is deposited on a structured substrate fabricated by nanoimprint lithography (NIL) to produce metal nanostructures.[26,27] Compared to the FON process, that using NIL has higher controllability of the resonance wavelength and larger freedom to design the location of hot spots. Furthermore, they have higher uniformity in large areas and higher reproducibility.

There have been many reports on the production of plasmonic substrates by metal deposition on structured substrates produced by NIL.[28–36] Li *et al.* produced a plasmonic substrate using gold (Au) deposition on a silica (SiO_2) pillar array prepared by NIL and achieved a high area-average SERS enhancement (1.2×10^9) and excellent uniformity (22.4% variation) in large area.[28]

Published under license by AIP Publishing.

Alvarez-Puebla *et al.* deposited a silver (Ag) island film on a silicon (Si) grating and a pillar array fabricated by NIL and studied the surface plasmon resonance behavior.[29] Yu *et al.* proposed a one-step direct nanoimprint-in-metal method to fabricate periodic structures on an Ag mirror and succeeded in detecting rhodamine 6G at concentration as low as 10^{-15} M by SERS.[30] Lee *et al.* proposed a hybrid approach combining NIL and a chemical deposition method to form an Ag microbead array for SERS and achieved the enhancement factor of 4.40×10^6 and the detection limit of 1.0×10^{-11} M.[33] Zhu *et al.* produced a plasmonic substrate by Au deposition on nanoimprinted polymer square nanopillars and nanoholes for the detection of lung cancer A549 cells, retinal pigment epithelial cells, and breast cancer MCF-7 cells and achieved cell detection in the range from 5×10^2 to 1×10^7 cells ml^{-1}.[35] Barbillon succeeded in detecting streptavidin as low as 10 pM in a biotin/streptavidin system by an Au nanodisk array on a glass substrate fabricated by NIL and a lift-off process.[36]

These previous reports indicate that metal deposition on structured substrates produced by NIL is a promising process to produce plasmonic substrates suitable for practical usages. However, in many cases, the mechanism of the high electric field enhancement and the location of hot spots are not very clear. Despite sharp plasmonic resonances predicted by simulations in plasmonic substrates prepared by NIL and metal disposition,[31,32] the measured reflection spectra are usually much broader,[28,29,31,32,34–36] and thus, calculated and measured reflection spectra hardly agree.[31,32] Therefore, the assignment of the electromagnetic mode contributing to the field enhancement and the identification of the location of the hot spots cannot be made by numerical simulations. This is an obstacle for further enhancement of the electric fields and for tuning the location of the hot spots.

The purpose of this work is to realize plasmonic substrates having surface plasmon resonances as sharp as those predicted by numerical simulations by a simple process, i.e., Au deposition on a commercially available nanoimprinted substrate. We show that by improving the roughness of the Au surface, the surface plasmon resonances become significantly sharp, and a very good agreement between experimental and calculated reflectance spectra is achieved. The good agreement allows us to identify the locations and field distributions of the hot spots. From the angle dependence of specular reflectance and diffuse reflectance measurements in combination with numerical simulations, we show that a dipolelike bright mode and a quadrupolelike dark mode exist at gaps between Au nanorods. Finally, we demonstrate the application of the developed plasmonic substrates for surface-enhanced fluorescence in sandwich immunoassays for the detection of influenza virus nucleoproteins. We show that the sharp resonance and the capability of precise tuning of the resonance wavelength of the plasmonic substrates result in strong enhancement of the fluorescence signal, which reduces the detection limit.

II. PREPARATION OF PLASMONIC SUBSTRATE

Figure 1(a) shows a schematic illustration of the process for the fabrication of a plasmonic substrate.[37] Polyolefin substrates with dome-shaped structures fabricated by nanoimprinting were purchased from SCIVAX (LP230/200-120). Figure 1(b) shows the scanning electron microscope (SEM) (FEI, HELIOS NANOLAB G3 UC) image of the nanoimprinted structure. The width, pitch, and height of the dome-shaped structures are 230 nm, 460 nm, and 200 nm, respectively. On the dome-shaped structures, Au thin films were deposited by electron-beam (EB) evaporation or sputtering. Figure 1(c) shows the SEM image after Au deposition (nominal thickness: 301 nm) by EB evaporation (EIKO) with the deposition rate of 1 Å/s, while Fig. 1(d) shows the SEM image after Au deposition (nominal thickness: 208 nm) by sputtering (SHIBAURA, i-millerII) in Ar gas (20 SCCM) at 50 W. We can see a clear difference in the morphology between the two methods: EB-deposited Au is bumpy, while sputter-deposited Au is smooth. The difference is explained by different kinetic energies of Au atoms during deposition.[38] The specular reflectance spectra (incident angle: 5°) (JASCO, V-670) of these substrates are shown in Fig. 1(e). The reflection loss below 500 nm is due to the interband transitions of Au. The EB-deposited substrate has a broad dip due to the surface plasmon resonance around 850 nm, while the sputter-deposited one has a

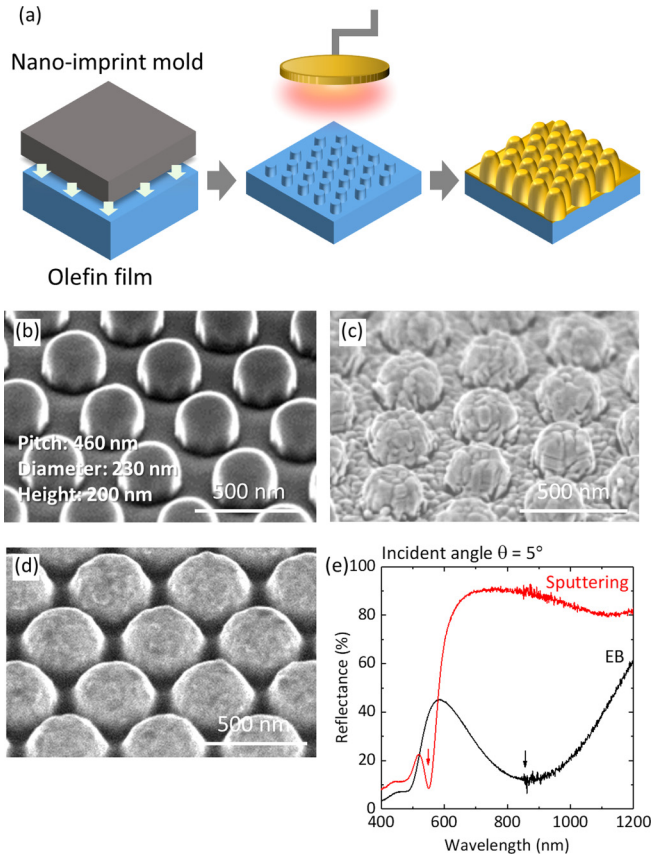

FIG. 1. (a) Schematic illustration of the plasmonic substrate fabrication process. (b) SEM image of a polyolefin substrate prepared using nanoimprinting. (c) and (d) SEM images after Au deposition: (c) EB and (d) sputtering. Nominal Au film thicknesses are 301 nm and 208 nm. (e) Reflectance spectra of the plasmonic substrates shown in (c) (black) and in (d) (red). Arrows indicate the surface plasmon resonance wavelengths. The incident angle is 5°.

Published under license by AIP Publishing.

sharp dip around 550 nm. Considering the very rough surface of the EB-deposited substrate, the broadening of the surface plasmon resonance is due to roughness. In this paper, in order to analyze the intrinsic property of the plasmonic substrate by excluding the effect of roughness, we will employ sputtering for the Au deposition.

III. RESULTS AND DISCUSSION

Figure 2 shows top (a), (c), (e), (g), (i) and cross-sectional (b), (d), (f), (h), (j) SEM images of plasmonic substrates. The Au deposition time and the nominal thickness are shown in the figures. The samples for cross-sectional observations were prepared by focused ion beam milling after coating the samples by C, Os, and Pt as protective layers. With increasing the Au deposition time, the diameter and height of Au pillars increase and the gap between adjacent Au pillars decreases. From the top view, we notice that the shape of Au pillars changes from round to hexagon, and the boundary between adjacent Au pillars changes from a point to a line. Since the gap between the pillars is a hot spot for the field enhancement as we will show later, the shape is an important factor to determine the field enhancement behavior.[28,39–41] In the longest deposition time (2143 s), adjacent Au pillars partially contact. In Fig. 2(k), the diameter, height, and gap length of Au nanostructures estimated from SEM images and the nominal Au thickness are plotted as a function of the sputtering time.

Figure 3 shows the measured specular reflectance spectra (incident angle: 5°) of the plasmonic substrates with different nominal Au film thicknesses. The spectrum of a flat Au film fabricated by sputter-deposition of Au on a flat substrate is shown as a reference. In the substrate with the thinnest Au (nominal thickness: 208 nm), a dip appears around 550 nm. The peak splits into two or three peaks with increasing thickness, and the long wavelength one shifts significantly to a longer wavelength. It is very plausible that the coupling of surface plasmons of adjacent Au nanostructures is the cause of the spectral change.[4,42,43] In the substrate with the thickest Au (nominal thickness: 488 nm), the surface plasmon resonances are broader than others. This may be due to partial contact of adjacent Au nanopillars as shown in the SEM image in Fig. 2(j).

In the application of a plasmonic substrate in fluorescence biosensing, utilizing near-infrared light for excitation and detection is preferable to avoid autofluorescence of biomolecules. In particular, due to the availability of light sources, phosphors, and detectors, the wavelength around 800 nm has been widely used. Therefore, in the following, we proceed to detailed analyses for the plasmonic substrate having the surface plasmon resonance around 800 nm. Note that since the resonance shifts about 50 nm after the formation of a sensor structure shown later, the resonance wavelength of a bare substrate should be around 750 nm. As can be seen in Fig. 3, this condition is satisfied when the nominal Au thickness is 386 nm.

In order to identify the surface plasmon resonance modes responsible for the reflection dips, we measure the angle dependence of the specular reflectance for p-polarized light (JASCO, V-670). Figure 4(a) shows the reflection spectra of the plasmonic substrate with the nominal Au thickness of 386 nm. The incident angle is changed from 5° to 75°. Figure 4(b) shows the contour map of the reflection spectra. We can see the existence of modes with a strong angle dependence and those almost independent of the angle. We

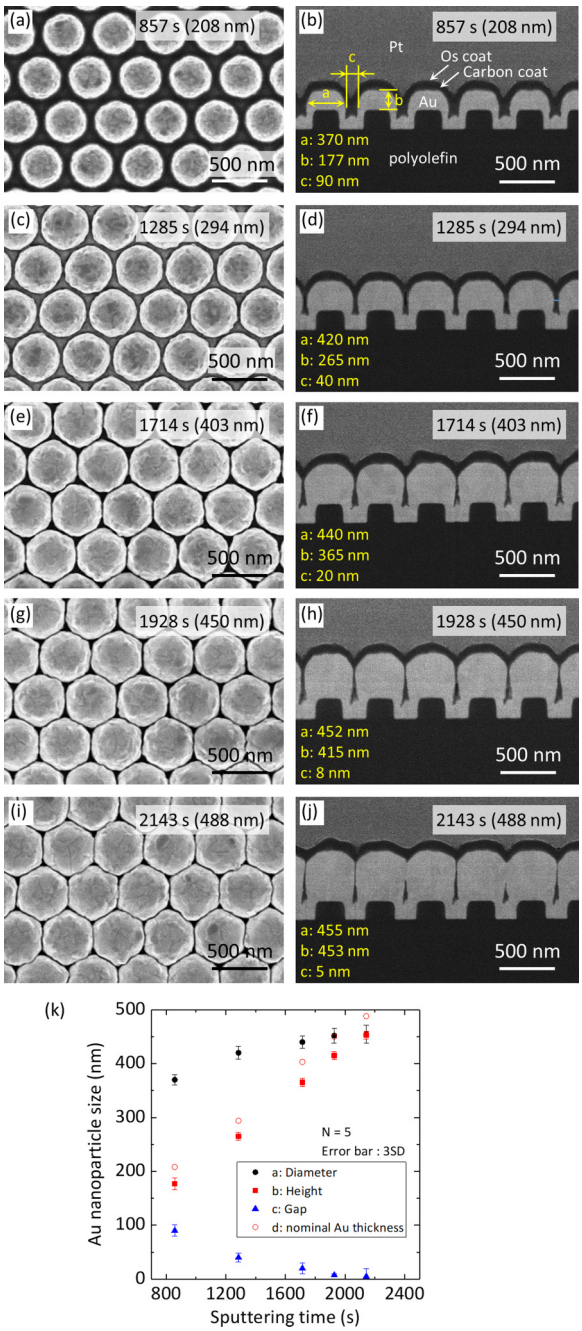

FIG. 2. (a), (c), (e), (g), and (i) Top and (b), (d), (f), (h), and (j) cross-sectional SEM images of plasmonic substrates prepared with different sputter-deposition time. The sputtering time and the nominal Au thickness are shown in the figures. C, Os, and Pt layers in the cross-sectional images are protective layers for the ion-milling process. a, b, and c in the cross-sectional images represent the definitions of the diameter, height, and gap length of Au nanostructures. The values of a, b, and c estimated from the images are shown in the figures. (k) Diameter (filled circle), height (filled square), and gap length (filled triangle) of Au nanostructures and nominal Au thickness (open circle) as a function of sputtering time.

Published under license by AIP Publishing.

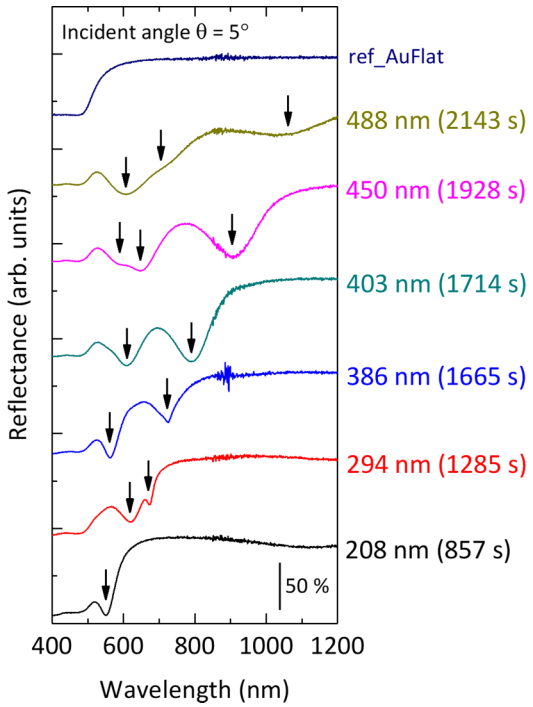

FIG. 3. Reflectance spectra of plasmonic substrates prepared with different sputter-deposition time. The sputtering time and the nominal Au thickness are shown in the figures. The incident angle is 5°. The data of the Au flat substrate are shown as a reference.

will discuss the dispersion relation later by comparing the experimental results with the simulation results.

In order to know the radiative and nonradiative nature of the observed plasmonic modes in the specular reflectance spectrum in Fig. 3, we distinguish the contributions of reflection, scattering, and absorption by measuring the specular and diffuse reflectance spectra of the same sample (nominal Au thickness: 386 nm). Figure 5(a) shows the measurement setups of specular and diffuse (SHIMAZU, SolidSpec-3700) reflectance spectra. The incident angle is 8° in both the measurements. In the specular reflectance, only the ratio of the reflected photons (R) with respect to the incident photons is measured, while in the diffuse reflectance geometry, that of the sum of the scattered (S) and reflected (R) photons are measured by using an integrating sphere. Therefore, by subtracting the specular reflection spectrum from the diffuse reflection spectrum, the ratio of the scattered photons (S) is obtained. Furthermore, by subtracting the diffuse reflection spectrum from 1, the ratio of absorbed photons (A) is obtained. Figure 5(b) shows diffuse (black) and specular (red) reflectance spectra, and Fig. 5(c) shows the scattering (blue) and absorpance (green) spectra. We can see that the scattering intensity of the 714 nm resonance is about twice larger than that of the 563 nm resonance, while the relation is vice versa in the absorpance. These results suggest that the surface plasmon mode with the resonance at 563 nm is a dark mode, while that with the resonance at

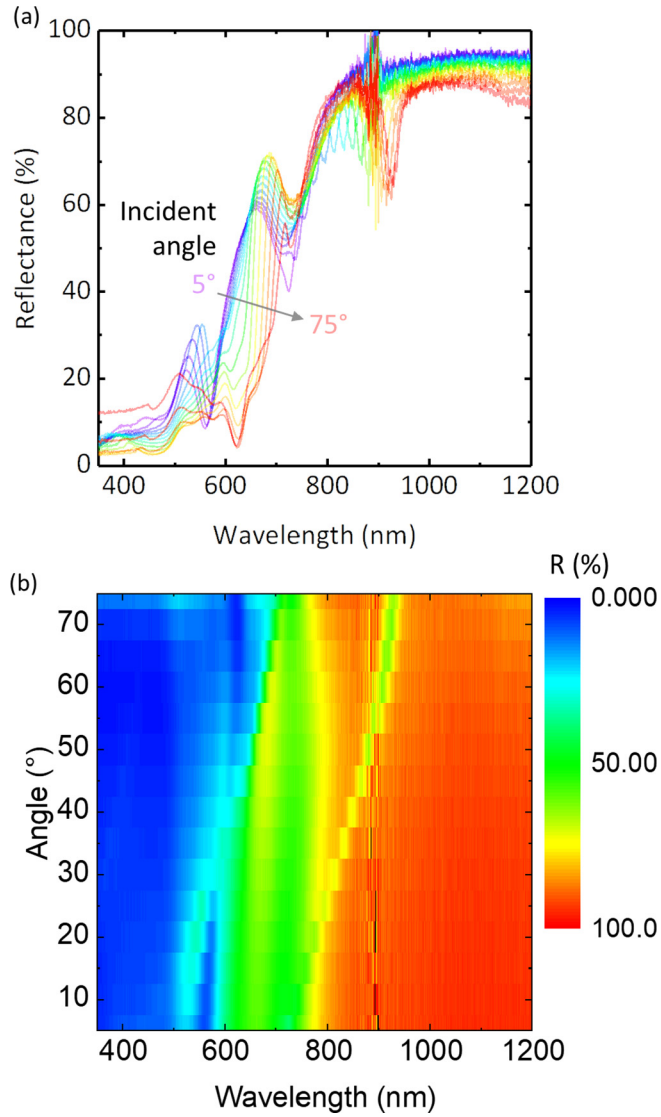

FIG. 4. (a) Incident angle dependence of reflectance spectra of a plasmonic substrate with the nominal Au thickness of 386 nm. The incident light is p-polarized. (b) The contour map of the reflectance spectra in (a).

714 nm is a bright mode. The validity of these assignments will be discussed later from the analyses of the electric field distributions.

We performed finite-difference time-domain (FDTD) simulations (Lumerical Solutions, Inc.) of the reflectance spectra and electric field distributions of a plasmonic substrate with the nominal Au thickness of 386 nm. The geometrical parameters are obtained from cross-sectional SEM images (see Fig. S1 in the supplementary material). Figure 6(a) shows the schematic illustration of the model structure used for the FDTD simulations. Au nanopillars composed of Au cylinders, and hemi-oblates are aligned hexagonally. The structural parameters are shown in the figure. The dielectric

Published under license by AIP Publishing.

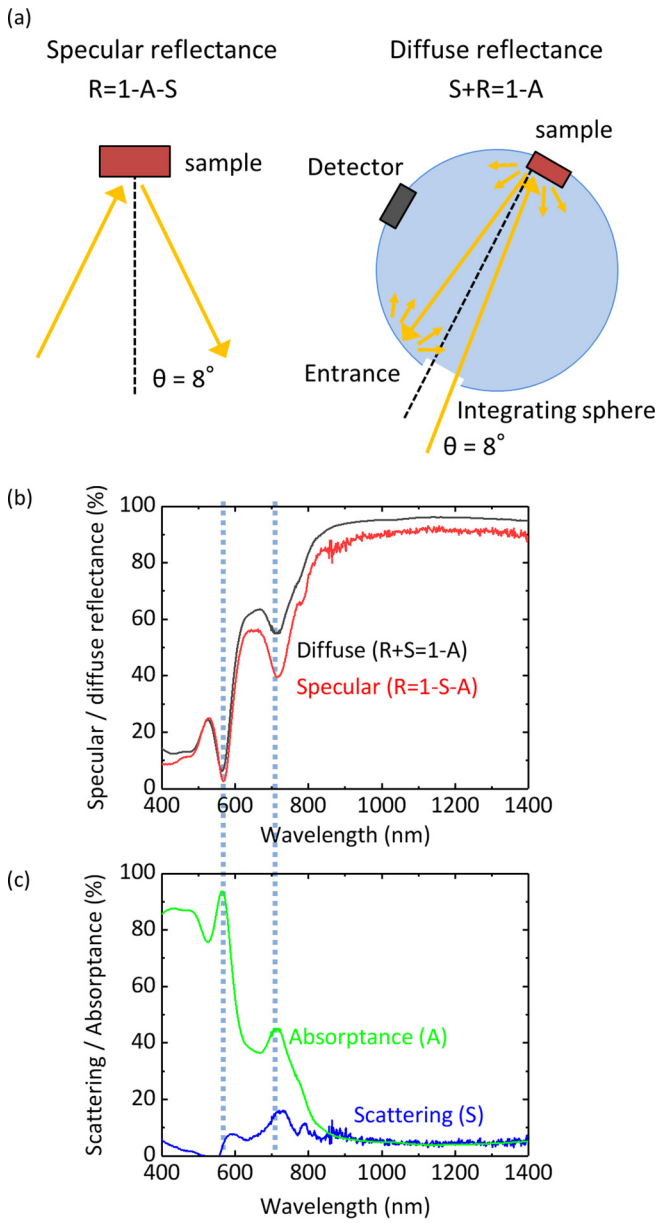

FIG. 5. (a) Schematic diagrams of specular and diffuse reflectance measurement setups. The incident angle is 8°. R, S, and A represent the ratios of reflected, scattered, and absorbed photons, respectively, with respect to the number of incident photons. (b) Diffuse (black) and specular (red) reflectance spectra of a plasmonic substrate with the nominal Au thickness of 386 nm. (c) Scattering (blue) and absorpance (green) spectra derived from specular and diffuse reflectance spectra.

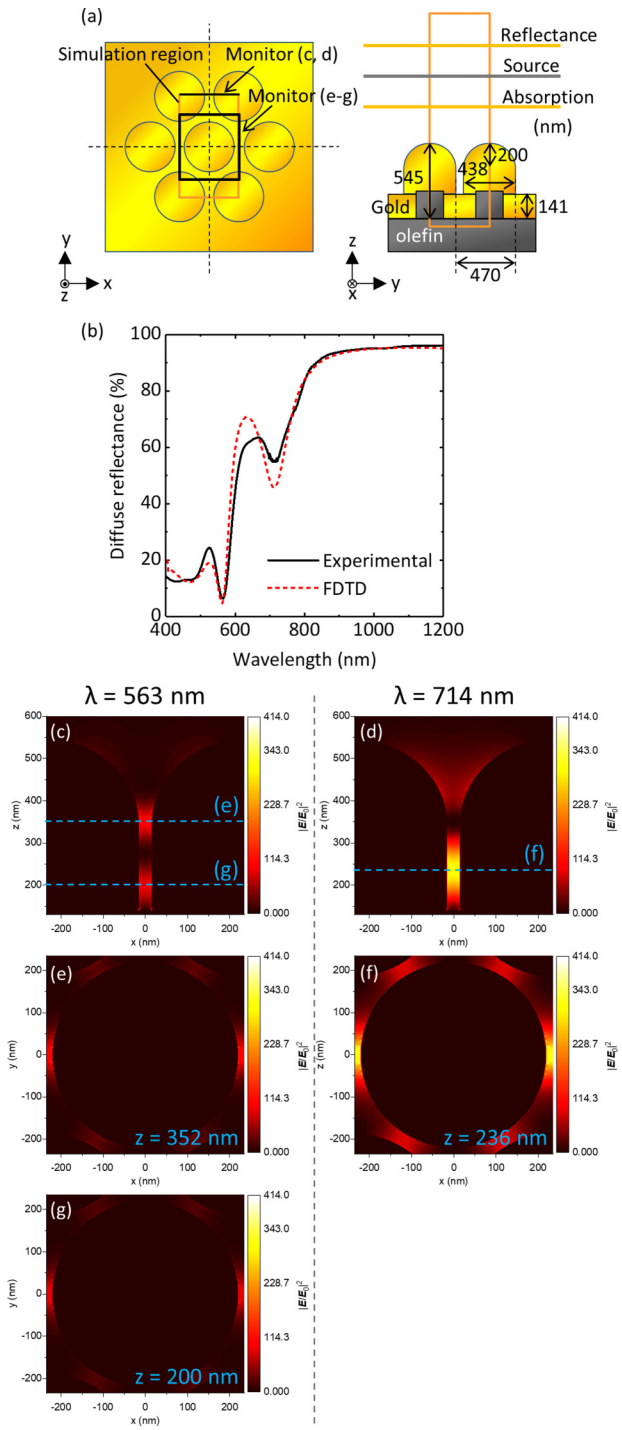

FIG. 6. (a) Schematic illustration of the model structure used for FDTD simulations. (b) Calculated spectrum of all reflected power (red) and measured diffuse reflectance spectrum (nominal Au thickness: 386 nm) (black). (c) and (d) XZ and (e)–(g) XY views of electric field intensity ($|\boldsymbol{E}/\boldsymbol{E}_0|^2$) at 563 nm (c), (e), (g) and at 714 nm (d) and (f).

function of Au is obtained from Johnson and Christy,[40] and the refractive indices of air and olefin are set to 1 and 1.55, respectively. The simulation region is defined by a unit cell consisting of one pillar and four quarter-pillars surrounded by periodic boundaries

Published under license by AIP Publishing.

(in-plane) and perfectly matched layers (out-of-plane). A linearly polarized plane wave light source, whose wave vector **k** is along the z-direction and the electric field vector **E** is along the x-direction, is placed above the nanopillar array to illuminate it. The absorbed power is calculated by a monitor placed between the source and the array, while all reflected power including reflection and scattering is calculated by a monitor placed above the source. Note that the calculated spectrum of all reflected power corresponds to the measured diffuse reflectance spectrum.

Figure 6(b) shows the calculated spectrum of all reflected power (red) for the model structure of a plasmonic substrate with the nominal Au thickness of 386 nm together with the measured diffuse reflectance spectrum (black) [the same spectrum as that in Fig. 5(b)]. We can see that the simulation reproduces the experimental spectrum very well. The resonance wavelengths agree almost perfectly. Furthermore, the depth and width of the 563 nm dip agree very well. A slight difference is the depth of the 714 nm dip; it is deeper in the simulation than in the experiment. It should be stressed here that the agreement between the experiment and the calculation in Fig. 6(a) is much better than those of previous work on similar structures.[4–6,31,32] The good agreement allows us to discuss the origin of the resonant modes from the electric field distributions.

Figures 6(c) and 6(d) show the xz cross sections of the electric field ($|\boldsymbol{E}/\boldsymbol{E}_0|^2$) at 563 nm and 714 nm, respectively. At 563 nm, two hot spots are formed around z = 200 nm and 352 nm in the gap between adjacent Au nanopillars. The maximum field enhancement factor is 186. On the other hand, only one hot spot (z = 236 nm) exists at 714 nm. The maximum field enhancement factor is 414, which is about 2.2-fold larger than that at 563 nm. The field distributions in the xz cross sections suggest that the resonance at 714 nm is a dipolelike lowest order cavity mode, while that at 563 nm is a higher-order multipole cavity mode.[4,44] Generally, the dipolelike mode is a bright mode being coupled to the far-field, while higher-order modes are dark modes with negligible far-field radiation.[45] As can be seen in the experimental absorpance and scattering spectra in Fig. 5(c), the 714 nm mode scatters light more than the 563 nm mode. This is consistent with the field distributions in Figs. 6(c) and 6(d) that the 714 nm mode is a dipolelike mode and the 563 nm mode is a higher-order mode. Figures 6(e)–6(g) show field distributions in the xy cross sections at the height of hot spots; (e) and (g) are at z = 352 nm and 200 nm, respectively, at 563 nm, and (f) is at z = 236 nm at 714 nm. The field distributions in the xy cross sections demonstrate that the hot spots exist at the gaps between adjacent Au nanostructures.

We also calculated the reflectance spectra in a wide incident angle (θ = 0°–70°) (see Fig. S2 in the supplementary material) and obtained the dispersion relation as shown in Fig. 7(a). The abscissa is an in-plane wave vector calculated from $k_{//} = (\omega/c)\ \sin\theta$. Similarly, Fig. 7(b) shows the dispersion relation obtained from the angle dependence of the specular reflectance in Fig. 4(a). We can see that the measured and calculated dispersion relations are very similar. This again demonstrates that the designed structure is produced almost perfectly. The dispersion relation reveals that the low energy mode has very small dispersion, while the high energy mode has relatively large dispersion. Therefore, the low energy mode is considered to be highly localized in the gap, while the high energy mode is a coupled mode reflecting the periodicity of the nanopillar lattice.[45–48]

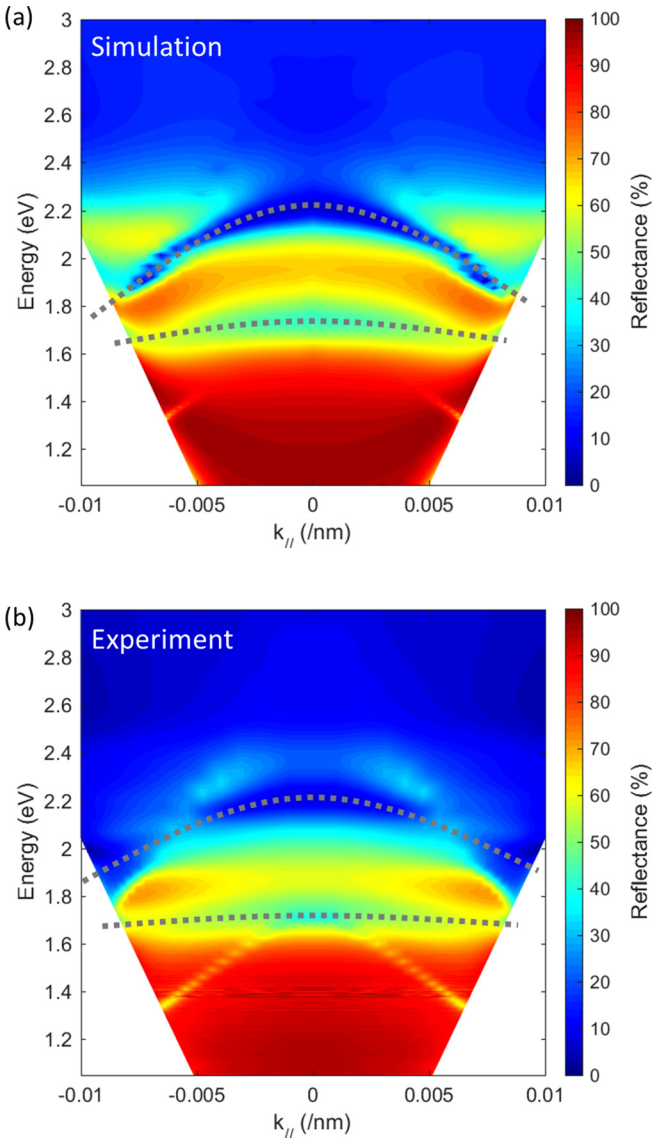

FIG. 7. (a) Simulated and (b) measured dispersion relations obtained from angle-resolved reflectance spectra. The measured dispersion relation is obtained from the data in Fig. 4(a).

Finally, we demonstrate the application of the developed plasmonic substrate to a sandwich immunoassay for the detection of influenza virus nucleoprotein (NP) by SEF. Figure 8(a) shows the schematic illustration of the immunoassay. Anti-influenza IgG antibody (abcam, ab66191), a capture antibody, was immobilized via self-assembled monolayer (SAM) on a plasmonic substrate. The nominal Au thickness in the plasmonic substrates is changed from 208 to 488 nm. Depending on the thickness, the wavelength of the

Published under license by AIP Publishing.

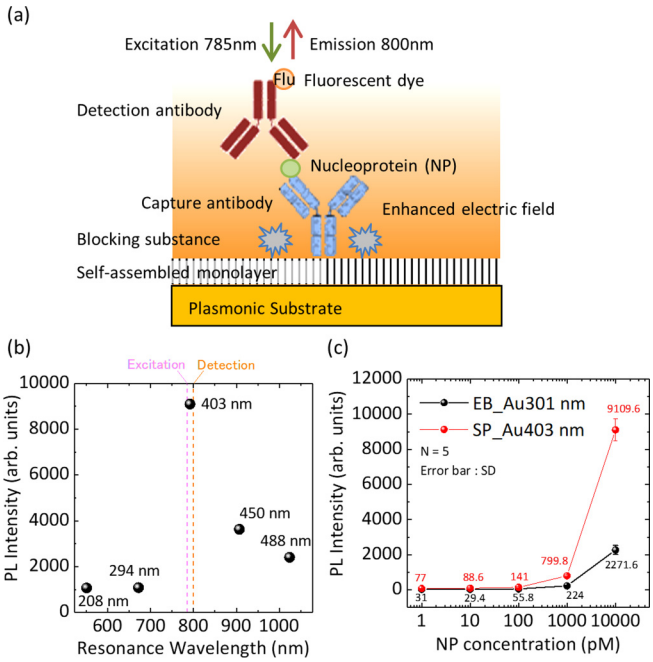

FIG. 8. (a) Schematic illustration of the sandwich immunoassay for the detection of influenza virus nucleoprotein using surface-enhanced fluorescence. (b) PL intensity of the sandwich immunoassay with a plasmonic substrate prepared by Au sputter-deposition. The abscissa is the surface plasmon resonance wavelength controlled by changing the Au thickness. The nominal Au thickness is shown in the figure. (c) PL intensity of the sandwich immunoassay as a function of nucleoprotein concentration. The data of plasmonic substrates produced by EB deposition (nominal Au thickness: 301 nm) and sputter-deposition (nominal Au thickness: 403 nm) are shown. The Au thicknesses are chosen so that the surface plasmon resonance wavelength becomes around 800 nm. The numbers in the figure correspond to the PL intensities.

dipolelike surface plasmon resonances changes from 550 nm to 1030 nm as shown in Fig. 3. If a recombinant influenza H1N1 NP (Sino Biological, 11675-V08B), an antigen, is captured by the IgG antibody, an anti-influenza IgG antibody (abcam, ac110661) labeled with an organic dye (Thermo Fisher, Dylight 800), a detection antibody, sandwiches the NP by an antigen-antibody reaction, and thus, the NP is detected by the photoluminescence (PL) of the organic dye. Figure 8(b) shows the PL intensity of the sandwich immunoassay [see Fig. S3 in the supplementary material for the PL spectra]. The abscissa is the resonance wavelength of the plasmonic substrates with different nominal Au thicknesses. The nominal thickness is shown in the figure. The excitation and detection wavelengths are 785 nm and 800 nm, respectively. The PL intensity is largely enhanced when the nominal Au thickness is 403 nm, i.e., when the resonance wavelength is close to the excitation and emission wavelengths.

We study the effects of surface roughness on the performance of the plasmonic substrates in the immunoassay by comparing the PL intensities between plasmonic substrates produced by EB deposition and sputter-deposition. As we already discussed in Fig. 1, the plasmonic substrate produced by EB deposition has a rough surface, while that produced by sputtering has a smooth surface. Figure 8(c) shows the PL intensity of a sandwich immunoassay as a function of NP concentration. The data of the plasmonic substrates produced by EB deposition (301 nm) and sputter-deposition (403 nm) are shown. The thicknesses are chosen so that the surface plasmon resonance wavelength is around 800 nm [see reflectance spectra in Fig. 1(e) (black) and in Fig. 3 (green)]. The numbers in the figure correspond to the PL intensities. Despite the almost same surface plasmon resonance wavelength, the PL intensity of the sandwich immunoassay with sputter-deposited Au is 2.5–4.0 times larger than that with EB-deposited Au in the whole NP concentration range. This suggests that the overall field enhancement at the resonant wavelength is larger in plasmonic substrates with a smoother surface.

IV. CONCLUSION

We have succeeded in achieving sharp surface plasmon resonances in plasmonic substrates prepared using nanoimprinting followed by Au sputter-deposition. The reflection spectra of the substrates could be well reproduced by numerical simulations. The good agreement between experiments and simulations allowed us to identify the locations and field distributions of the hot spots. The angle dependence of specular reflectance and diffuse reflectance measurements in combination with numerical simulations reveal that a dipolelike bright mode and a higher-order dark mode exist at gaps between Au nanopillars. Finally, we demonstrate the application of the developed plasmonic substrates for surface-enhanced fluorescence in sandwich immunoassays for the detection of influenza virus nucleoprotein. We show that the sharp resonance and the capability of precise tuning of the resonance wavelength of the plasmonic substrates with a smooth metal surface result in strong enhancement of the luminescence signal.

SUPPLEMENTARY MATERIAL

See the supplementary material for the modeling of an Au nanopillar array in FDTD simulations and calculated angle-resolved specular reflectance spectra.

ACKNOWLEDGMENTS

This work was partly supported by JSPS KAKENHI under Grant Nos. 16H03828, 18K14092, and 18KK0141.

REFERENCES

[1] S. Lal, S. Link, and N. J. Halas, *Nanoscience and Technology* (World Scientific, 2009), pp. 213–220.
[2] M. Li, S. K. Cushing, and N. Wu, Analyst **140**, 386 (2015).
[3] C. L. Haynes and R. P. Van Duyne, J. Phys. Chem. B **107**, 7426 (2003).
[4] Y. Huang, X. Zhang, J. Li, L. Ma, and Z. Zhang, J. Mater. Chem. C **5**, 6079 (2017).
[5] Y. Huang, X. Zhang, E. Ringe, L. Ma, X. Zhai, L. Wang, and Z. Zhang, Nanoscale **10**, 4267 (2018).
[6] Y. Huang, X. Zhang, E. Ringe, M. Hou, L. Ma, and Z. Zhang, Sci. Rep. **6**, 23159 (2016).
[7] T. Siegfried, Y. Ekinci, O. J. F. Martin, and H. Sigg, Nano Lett. **13**, 5449 (2013).

Published under license by AIP Publishing.

[8]A. Kinkhabwala, Z. Yu, S. Fan, Y. Avlasevich, K. Müllen, and W. E. Moerner, Nat. Photonics **3**, 654 (2009).
[9]R. M. Bakker, H.-K. Yuan, Z. Liu, V. P. Drachev, A. V. Kildishev, V. M. Shalaev, R. H. Pedersen, S. Gresillon, and A. Boltasseva, Appl. Phys. Lett. **92**, 043101 (2008).
[10]Z.-J. Yang, Z.-S. Zhang, L.-H. Zhang, Q.-Q. Li, Z.-H. Hao, and Q.-Q. Wang, Opt. Lett. **36**, 1542 (2011).
[11]M. Kawasaki and S. Mine, J. Phys. Chem. B **109**, 17254 (2005).
[12]J. R. Lakowicz, Anal. Biochem. **298**, 1 (2001).
[13]M. Shioi, H. Jans, K. Lodewijks, P. Van Dorpe, L. Lagae, and T. Kawamura, Appl. Phys. Lett. **104**, 243102 (2014).
[14]J. S. Biteen, N. S. Lewis, H. A. Atwater, H. Mertens, and A. Polman, Appl. Phys. Lett. **88**, 131109 (2006).
[15]P. P. Pompa, L. Martiradonna, A. Della Torre, F. Della Sala, L. Manna, M. De Vittorio, F. Calabi, R. Cingolani, and R. Rinaldi, Nat. Nanotechnol. **1**, 126 (2006).
[16]A. G. Brolo, S. C. Kwok, M. D. Cooper, M. G. Moffitt, C. W. Wang, R. Gordon, J. Riordon, and K. L. Kavanagh, J. Phys. Chem. B **110**, 8307 (2006).
[17]T. R. Jensen, M. D. Malinsky, C. L. Haynes, and R. P. Van Duyne, J. Phys. Chem. B **104**, 10549 (2000).
[18]E. M. Hicks, X. Zhang, S. Zou, O. Lyandres, K. G. Spears, G. C. Schatz, and R. P. Van Duyne, J. Phys. Chem. B **109**, 22351 (2005).
[19]M. Shioi, K. Lodewijks, L. Lagae, T. Kawamura, and P. Van Dorpe, Appl. Phys. Lett. **97**, 163106 (2010).
[20]J. P. Camden, J. A. Dieringer, J. Zhao, and R. P. Van Duyne, Acc. Chem. Res. **41**, 1653 (2008).
[21]Y. Mochizuki, M. Fujii, S. Hayashi, T. Tsuruoka, and K. Akamatsu, J. Appl. Phys. **106**, 013517 (2009).
[22]W.-C. Lin, L.-S. Liao, Y.-H. Chen, H.-C. Chang, D. P. Tsai, and H.-P. Chiang, Plasmonics **6**, 201 (2011).
[23]C. Farcău and S. Aştilean, Appl. Phys. Lett. **95**, 193110 (2009).
[24]H. Sugimoto, S. Yashima, K. Furuta, A. Inoue, and M. Fujii, Appl. Phys. Lett. **108**, 241103 (2016).
[25]A. Inoue, H. Sugimoto, and M. Fujii, J. Phys. Chem. C **121**, 11609 (2017).
[26]S. Y. Chou, J. Vac. Sci. Technol. B **14**, 4129 (1996).
[27]L. J. Guo, Adv. Mater. **19**, 495 (2007).
[28]W.-D. Li, F. Ding, J. Hu, and S. Y. Chou, Opt. Express **19**, 3925 (2011).
[29]R. Alvarez-Puebla, B. Cui, J. P. Bravo-Vasquez, T. Veres, and H. Fenniri, J. Phys. Chem. C **111**, 6720 (2007).
[30]C.-C. Yu, Y.-C. Tseng, P.-Y. Su, K.-T. Lin, C.-C. Shao, S.-Y. Chou, Y.-T. Yen, and H.-L. Chen, Nanoscale **7**, 3985 (2015).
[31]A. M. Lopatynskyi, V. K. Lytvyn, V. I. Nazarenko, L. J. Guo, B. D. Lucas, and V. I. Chegel, Nanoscale Res. Lett. **10**, 99 (2015).
[32]R. D. Nagel, S. Filser, T. Zhang, A. Manzi, K. Schönleber, J. Lindsly, J. Zimmermann, T. L. Maier, G. Scarpa, K. Krischer, and P. Lugli, J. Appl. Phys. **121**, 084305 (2017).
[33]T. Lee, S. Jung, S. Kwon, W. Kim, J. Park, H. Lim, and J. Lee, Sensors **19**, 1046 (2019).
[34]T. Matsushita, T. Nishikawa, H. Yamashita, R. Hasui, S. Fujita, and Y. Okuno, Jpn. J. Appl. Phys. **47**, 7420 (2008).
[35]S. Zhu, H. Li, M. Yang, and S. W. Pang, Nanotechnology **27**, 295101 (2016).
[36]G. Barbillon, Micromachines **3**, 21 (2012).
[37]H. Yanagawa, A. Inoue, H. Sugimoto, M. Shioi, and M. Fujii, J. Appl. Phys. **122**, 223101 (2017).
[38]J. M. Lackner, W. Waldhauser, A. Alamanou, C. Teichert, F. Schmied, L. Major, and B. Major, Bull. Pol. Acad. Sci. Tech. **58**, 281 (2010).
[39]S. L. Kleinman, B. Sharma, M. G. Blaber, A.-I. Henry, N. Valley, R. G. Freeman, M. J. Natan, G. C. Schatz, and R. P. Van Duyne, J. Am. Chem. Soc. **135**, 301 (2013).
[40]P. B. Johnson, and R. W. Christy, Phys. Rev. **6**(12), 4370–4379 (1972).
[41]J. P. Litz, J. P. Camden, and D. J. Masiello, J. Phys. Chem. Lett. **2**, 1695 (2011).
[42]M. D. Doherty, A. Murphy, R. J. Pollard, and P. Dawson, Phys. Rev. X **3**, 011001 (2013).
[43]D. P. Lyvers, J.-M. Moon, A. V. Kildishev, V. M. Shalaev, and A. Wei, ACS Nano **2**, 2569 (2008).
[44]N. G. Bastús, J. Piella, and V. Puntes, Langmuir **32**, 290 (2016).
[45]T. K. Hakala, H. T. Rekola, A. I. Väkeväinen, J.-P. Martikainen, M. Nečada, A. J. Moilanen, and P. Törmä, Nat. Commun. **8**, 13687 (2017).
[46]G. Lozano, D. J. Louwers, S. R. Rodríguez, S. Murai, O. T. Jansen, M. A. Verschuuren, and J. Gómez Rivas, Light Sci. Appl. **2**, e66 (2013).
[47]R. Guo, S. Derom, A. I. Väkeväinen, R. J. A. van Dijk-Moes, P. Liljeroth, D. Vanmaekelbergh, and P. Törmä, Opt. Express **23**, 28206 (2015).
[48]S. R. K. Rodriguez, A. Abass, B. Maes, O. T. A. Janssen, G. Vecchi, and J. Gómez Rivas, Phys. Rev. X **1**, 021019 (2011).

Published under license by AIP Publishing.